JOURNAL OF PROPULSION AND POWER
Vol. 26, No. 4, July–August 2010

Technical Notes

Numerical Study of Supersonic Combustion Processes with Central Strut Injection

Marius C. Banica,* Tobias Scheuermann,† Jaechul Chun,†
Bernhard Weigand,‡ and Jens von Wolfersdorf‡
Universität Stuttgart, 70569 Stuttgart, Germany

DOI: 10.2514/1.43599

Nomenclature

A	=	area, m^2
c	=	speed of sound, m/s
M	=	Mach number, u/c
$\dot{m}$	=	mass flow rate, kg/s
p	=	pressure, N/m^2
T	=	temperature, K
u	=	axial velocity, m/s
Y	=	mass fraction, ρ_i/ρ_{gas}
y^+	=	distance of the centers of wall cells from the wall
α	=	weighting factor
η_c	=	combustion efficiency
η_m	=	mixing efficiency
ρ	=	density
ϕ	=	equivalence ratio

Subscripts

0	=	stagnation conditions
i	=	species

I. Introduction

WE REPORT on numerical studies of the flow conditions in the supersonic combustion facility of the Institute of Aerospace Thermodynamics of the Universität Stuttgart. For all calculations, the commercial tool CFD++ was used. The aim was to determine whether a design-study-oriented approach can be used to analyze different combustion modes in comparison with experimental data.

II. Combustion Chamber

The combustion chamber is shown in Fig. 1. It has a rectangular cross section with width $w = 40$ mm and constant isolator height $h = 35.4$ mm. Downstream distance, x, is measured from the Laval nozzle throat where $x = 0$. Air enters the chamber from the left at a Mach number of $M = 2.1$ at isolator entry. The combustor and diverging sections open at angles $\alpha_1 = 1°$ and $\alpha_2 = 2°$, respectively. The outflow static pressure is $p_\infty \approx 0.96$ bar. The facility operates continuously at stagnation conditions $T_{0,\text{air}} = 1400$ K and $p_{0,\text{air}} = 4$ bar. For brevity, in the following, wall pressures in the symmetry plane are only shown for the upper wall. Our injector is shown in Fig. 1b. Chun et al. [1] provide further details about the facility and Gerlinger et al. [2,3] provide further details on the injector. Because of exploitation of symmetry, only half the channel width is modeled. H_2 is injected through the horizontal slots (see Fig. 1b). At design conditions, the injection Mach number is $M_{H_2} = 2.6$. However, in practice, this is probably not achieved, due to geometric deformation. As a conservative estimate we chose $M_{H_2} = 1.0$. The validity of this choice is checked in Sec. V.E. Four combustion modes, i.e., blowoff, weak combustion, strong combustion, and thermal choking were observed. Because of flow overexpansion, all modes feature a shock train in proximity of the channel outflow. Another shock train develops in the isolator, due to injector displacement effects. In flight, strong combustion is desired. Here, the injector acts as the flame holder and heat release is high. For weak combustion the fuel–air mixture is ignited in the outflow shock train. The flame is detached from the injector and heat release is significantly lower. If, in these conditions, the exit pressure is lowered sufficiently, the outflow shock train disappears, and combustion ceases (blowoff). For excessive fuel injection, the flow becomes thermally choked. The combustion mode is determined by the geometry, stagnation conditions, ambient pressure, and the global equivalence ratio ϕ (see also Scheuermann et al. [4]).

III. Numerical Simulations

The numerical tool used is CFD++ [5] and was extensively validated by Goldberg et al. [6–9] and Palaniswamy et al. [10]. Discretization is formally second order with a shear stress transport turbulence model. All simulations are steady state using a Courant–Friedrichs–Lewy number of 20. Hydrogen combustion was modeled by the scheme of Gerlinger et al. [11]. Turbulence-chemistry interactions were neglected. As a result, we expect some deficiencies in the prediction of ignition delay times. However, we show below that in our setup ignition occurs in local subsonic recirculation zones. Therefore, turbulence–chemistry interactions should not play a crucial role. In the numerical domain, the throat of the Laval nozzle marked the air inflow. The outflow corresponded to the physical outflow. The injected hydrogen mass flow $\dot{m}_{H_2,\text{inj}}$ was varied systematically with regard to the reference point from Table 1. The equivalence ratio is defined as

$$\phi = \frac{\dot{m}_{H_2,\text{inj}}}{\dot{m}_{H_2,\text{st}}} \tag{1}$$

where $\dot{m}_{H_2,\text{st}}$ is the stoichiometric hydrogen mass flow rate. In the reference case $\phi = 0.27$ and the Reynolds number at isolator inflow $Re = 4.98 \times 10^5$ based on the isolator hydraulic diameter. Walls were isothermal with $T_c = 400$ K and $T_i = 600$ K for the channel and injector, respectively. The influence of wall temperatures is analyzed in Sec. V.F. Based on experimental data, we estimate the total temperature of hydrogen as $T_{0,H_2} = 400$ K. The total pressure p_{0,H_2} was used to control $\dot{m}_{H_2,\text{inj}}$. For all parameter studies we used grid G1 (see Table 2). Figure 1b shows details of G1 in the injector vicinity. Grid independence was checked by computing the problem on three finer grids, i.e., G2, G3, and G4. Except for G4, all grids were used with wall functions. As a cross check, we resolved the boundary layers directly on G4 so that $y^+ < 1$ in the first cell center near the walls. However, to limit runtimes, the domain for G4 only included $x \leq 0.75$ m. We report the results of the grid sensitivity studies in Sec. V.F.

Received 3 February 2009; revision received 11 February 2010; accepted for publication 22 February 2010.

*Postdoctoral Researcher, Institute for Aerospace Thermodynamics, Pfaffenwaldring 31.
†Ph.D. Student, Institute for Aerospace Thermodynamics, Pfaffenwaldring 31.
‡Professor, Institute for Aerospace Thermodynamics, Pfaffenwaldring 31.

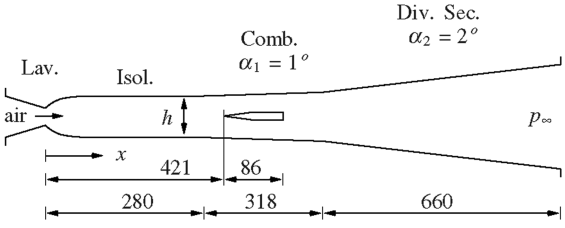

a)

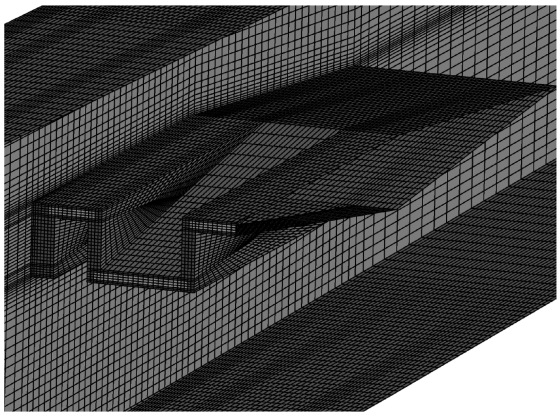

b)

Fig. 1 Illustrations of a) experimental facility (lengths in mm, Lav. is the laval nozzle, Isol. is the isolator, Comb. is the combustor, and Div. Sec. is the diverging section) and b) injector and grid.

IV. Performance Parameters

The performance of the combustion chamber is characterized by means of two parameters. The first is the mixing efficiency η_m. Using the definition given by Gerlinger et al. [3],

$$\eta_m(x) = \frac{\int_A \alpha \rho_{\text{gas}} Y_{\text{H}_2} u \, \mathrm{d}A}{\int_A \rho_{\text{gas}} Y_{\text{H}_2} u \, \mathrm{d}A} = \frac{\int_A \alpha \rho_{\text{gas}} Y_{\text{H}_2} u \, \mathrm{d}A}{\dot{m}_{\text{H}_2}(x)} \quad \text{with}$$

$$\alpha = \begin{cases} 1/\phi: & \phi \geq 1, \\ 1: & \phi < 1 \end{cases} \tag{2}$$

where ρ_{gas} is the gas density, Y_{H_2} is the mass fraction of hydrogen with $Y_{\text{H}_2} = \rho_{\text{H}_2}/\rho_{\text{gas}}$, ρ_{H_2} is the density of hydrogen, A is the cross-sectional area, and u is the axial velocity. Here, ϕ is the local equivalence ratio:

$$\phi = \frac{1}{2} \frac{M_{\text{O}_2}}{M_{\text{H}_2}} \frac{Y_{\text{H}_2}}{Y_{\text{O}_2}} \tag{3}$$

Table 1 Reference case (strong combustion, $\phi = 0.27$)

	Air	Hydrogen
p, kPa	211.2	111.0
T, K	1166	333.33
u, m/s	684.5	1385.9
A, m^2	8.042×10^{-4}	2.576×10^{-5}
M	1	1
$\dot{m}$, kg/s	0.3471	2.886×10^{-3}

Table 2 Grids for convergence studies

Grid	Cells	Wall treatment	Determinant	Aspect Ratio
G1	1,056,928	Wall function	≥ 0.738	≤ 36
G2	2,517,032	Wall function	≥ 0.731	≤ 34
G3	3,355,558	Wall function	≥ 0.724	≤ 32
G4	3,996,790	Integration	≥ 0.761	≤ 1780

where M_{H_2} and M_{O_2} are the molecular weights of hydrogen and oxygen, respectively, and Y_{O_2} is the mass fraction of oxygen. The second parameter is the combustion efficiency:

$$\eta_c(x) = 1 - \frac{\int_A \rho_{\text{gas}} Y_{\text{H}_2} u \, \mathrm{d}A}{\dot{m}_{\text{H}_2,\text{inj}}} \tag{4}$$

which describes how much of the injected fuel has been consumed since injection.

V. Results

A. Flowfield

In strong combustion, the flame is stabilized by subsonic recirculation zones in the wake of the injector. Separated flow regions also develop in the channel corners above and below the injector leading and trailing edges. The separation around the leading edges is caused by injector displacement effects and therefore present in the absence of combustion. However, the separation around the injector trailing edges is a feature of strong combustion and disappears for weak combustion or blowoff. During strong combustion, the flame ignites in the immediate wake of the vertical ligaments. This is evident from the static temperature distributions given in Fig. 2a. T increases significantly in the immediate wake of the injector and for small x, we observe hot combustion products in close vicinity of the sidewall. For larger x, the flame remains in the center of the channel. Peak values for T are

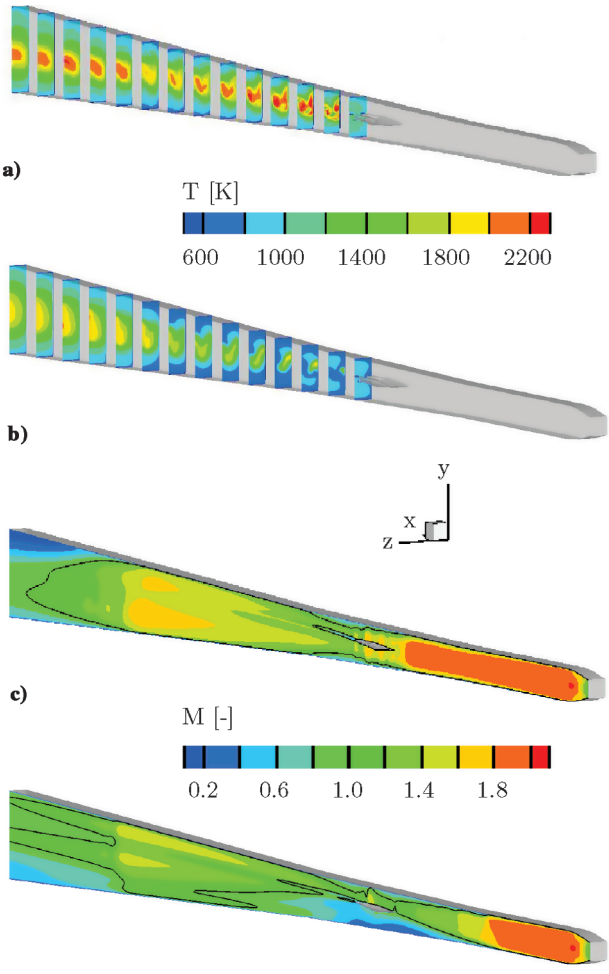

Fig. 2 Illustrations of a) T for strong combustion in the reference case $\phi = 0.27$, b) T for weak combustion at $\phi = 0.13$, c) M for strong combustion in the reference case $\phi = 0.27$, and d) M for thermal choking at $\phi = 1.32$ including isoline $M = 1$.

in excess of 2200 K. Figure 2b shows similar distributions for operation under weak combustion at $\phi = 0.13$. Here, T also rises in the wake of the injector and some fuel is consumed in the vicinity of the sidewall. Around the outflow the local shock train reignites the fuel–air mixture. However, both peak and local values of T are significantly lower than for the reference case. Figure 2c shows the distribution of M in the symmetry plane for the reference case. Also indicated is the sonic line. Evidently, most of the flow is supersonic. The same is true for cross sections closer to the wall. We also observe a region of separated flow on the upper wall around the outflow, which is associated with the outflow shock train.

B. Wall Pressure Distributions

1. Air Injection ($\phi = 0$)

Figure 3a shows $\tilde{p}$ when air is injected at $T_0 = 400$ K, $p_0 = 4$ bar, and $M = 1$. All values are normalized as follows:

$$\tilde{p} = \frac{p_w(x)}{\bar{p}_0(x = 0)} \tag{5}$$

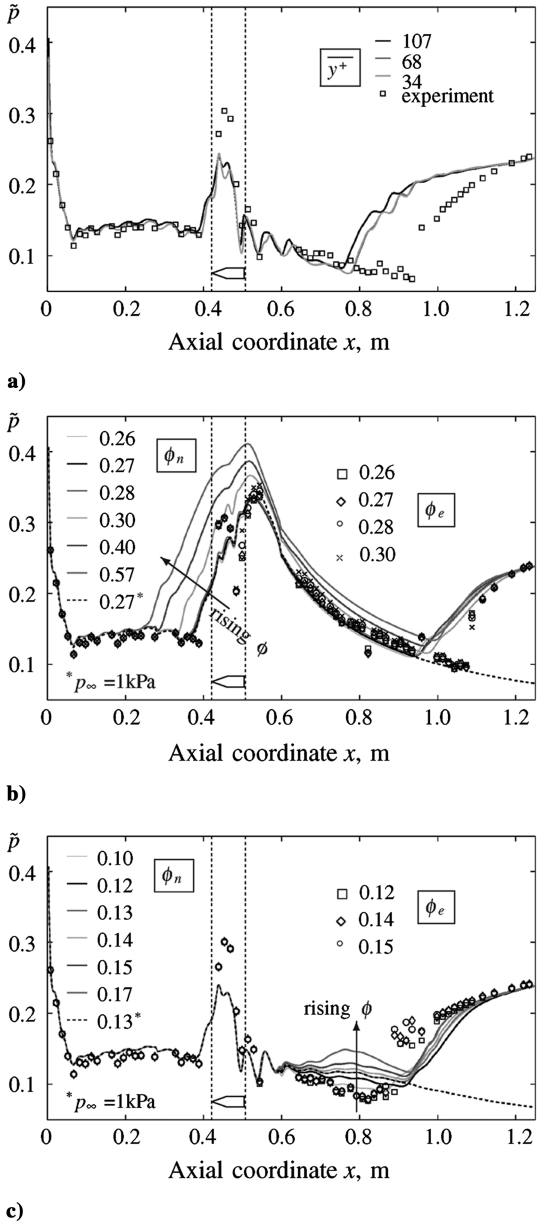

Fig. 3 Plots of $\tilde{p}$ for a) air injection, b) strong combustion, and c) weak combustion at different ϕ; numerical simulations (ϕ_n) and experiment (ϕ_e).

where $p_w(x)$ is the wall static pressure. Numerical data are represented by curves and experimental data are represented by symbols. The figure contains data for several averaged $\bar{y}^+$. All calculations were on G1. The sharp decrease in pressure for very small x is due to the expansion of the flow in the Laval nozzle. Further downstream, there is a regular pattern of pressure variations followed by a steep pressure increase just upstream of the injector. These features are generated by the isolator shock train. The pressure variations around the injector are in part generated by a complicated local system of shocks and expansion waves described by Gerlinger et al. [3]. The increase in pressure around $x \approx 0.78$ m (for the numerical data) is due to the outflow shock train. The numerical results match the experimental data reasonably well except in the vicinity of the outflow shock train and around the injector. The flow here is dominated by shocks, shock/boundary-layer interactions and the development of recirculation zones. The use of wall functions then poses obvious limits to the numerical accuracy. Furthermore, turbulence behind shock waves can be strongly nonisotropic, which any two-equation closure fails to describe. Finally, we note that for the largest value $\bar{y}^+ = 107$, the distributions are slightly different than for the two smaller values $\bar{y}^+ = 68$ and $\bar{y}^+ = 34$. These differences are greater close to the outflow shock train and are also observable around the injector. In the remaining channel, the distributions are virtually identical. This suggests that $\bar{y}^+$ has a small influence on the results. Therefore, we refrained from optimizing the value for each computation.

2. Strong Combustion and Thermal Choking ($\phi > 0.26$)

Numerical and experimental results for $\tilde{p}$ in strong combustion are given in Fig. 3b for various ϕ. Compared with Fig. 3a, the distributions show a large rise in pressure in the immediate wake of the injector, due to the heat release from combustion. The predictions match the experimental data reasonably well, except around the injector and in the vicinity of the outflow shock train. The reasons for this are the same as described above for the injection of air. To show that the outflow shock train is due to the overexpansion, we calculated a case with $p_\infty = 1$ kPa at the reference $\phi = 0.27$. The results are given by the dashed line in Fig. 3b. The steep increase around $x \approx 0.94$ m has disappeared and the flow is now underexpanded, leading to a smooth decrease in pressure in the diverging part. For high ϕ, combustion begins to affect flow conditions upstream of the injector. This is the case for all $\phi > 0.28$. The heat release here is excessively large and the isolator shock train becomes gradually stronger, while M upstream of the injector decreases. For still larger ϕ, subsonic flow regions appear in the isolator. This condition can be interpreted as thermal choking. However, we never observed an entirely subsonic flow in the isolator and inflow unstart never occurred. An example of the Mach number distribution for high ϕ is shown in Fig. 2d for $\phi = 1.32$. Also shown is the sonic line. Clearly, the flow is partly supersonic upstream of the injector and the shock system remains isolated from the nozzle. Flame ignition can be analyzed more closely by considering the distribution of OH radicals (see Fig. 4a). There are regions of high chemical activity in the wake of the vertical ligaments. These constitute ignition cores and are associated with the local recirculation zones. From these cores, the flame grows and occupies increasingly large areas of the cross sections.

3. Weak Combustion and Blowoff ($\phi < 0.17$)

Figure 3c shows $\tilde{p}$ for weak combustion at various ϕ. When compared with Fig. 3b, the pressure rise around the injector trailing edges has disappeared, since the heat release is much lower. The distributions are similar to the results for air injection. Furthermore, the reduced pressures around the downstream half of the injector indicate that strong combustion influences the flowfield upstream of injection. The general trends are reproduced by the numerics, but there are discrepancies in isolated regions. In the vicinity of the injector and around the outflow shock train these can probably be linked to the issues described before. However, the discrepancies in the region 0.59 m $< x <$ 0.93 m have a different origin. Here, the

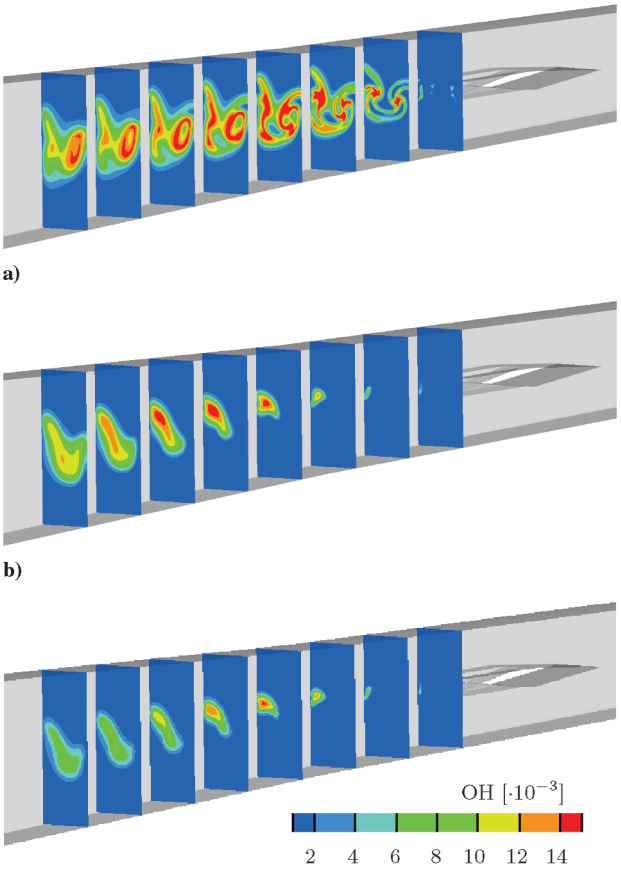

Fig. 4 Illustrations of a) distributions of OH in the reference case at $\phi = 0.27$, b) weak combustion at $\phi = 0.17$, and c) weak combustion at $\phi = 0.13$.

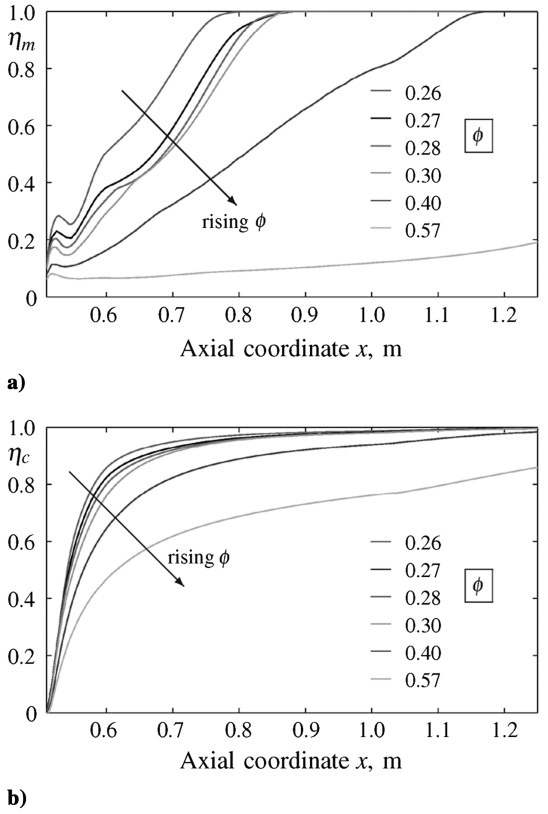

Fig. 5 Plots of a) η_m and b) η_c for various ϕ with strong combustion.

predicted increase in pressure with rising ϕ is not found in the experiments. Rather, in reality, fuel is almost exclusively consumed in the outflow shock train. In the simulation, however, the fuel is partly consumed upstream of the outflow shock train, which is also evident from Figs. 2b, 4b, and 4c. The latter two show the distribution of OH radicals in the injector wake for $\phi = 0.13$ and 0.17, respectively: i.e., two cases of weak combustion. Here, the fuel–air mixture ignites in the wall boundary layer behind the vertical ligament of the injector. The experiment provided optical access to this area and the observations did not show flame ignition here. Hence, for weak combustion, the simulation predicts ignition different than found in the experiment. As before, we also computed one case with $p_\infty = 1$ kPa. These data are represented by the dashed curve in Fig. 3c for $\phi = 0.13$.

4. *Intermediate Range* ($0.18 < \phi < 0.25$)

A transition between weak and strong combustion appears in the experiments at $\phi \approx 0.20$ when ϕ is increased from low to high values. This transition was investigated experimentally in earlier studies [1,4]. However, at present, the transition mechanism is not fully understood and the simulations show significant oscillations in convergence behavior for this range.

C. Mixing Efficiency

Figure 5a shows η_m for several ϕ in strong combustion. In the near field, we observe a significant decrease in mixing performance with increasing ϕ, since higher fuel mass flow rates place more severe demands on the efficiency of the mixing process. For larger x, mixing eventually becomes complete for all cases except $\phi = 0.57$. Here, excessive amounts of fuel are injected and not all of it can be mixed rapidly enough with the air to allow its consumption. Significant amounts of fuel then remain trapped in the cores of the generated streamwise vortices. This leads to permanent local equivalence ratios larger than 1 and places a limit $\phi_m^{\max}$ on the amount of fuel that can be mixed; $\phi_m^{\max}$ is a function of the geometry and operating point. Here, we find $\phi_m^{\max} \approx 0.40$.

D. Combustion Efficiency

Figure 5b shows η_c for several ϕ in strong combustion. For $\phi \leq 0.30$ more than 91% of the injected fuel is consumed within the first 20 cm downstream of injection. This is largely due to the rapid mixing provided by the injector and would allow the design of very short combustion chambers with reduced frictional drag. Alternatively, a second injection stage could be introduced to exploit the remaining oxygen. Generally, we find a decrease in η_c for higher ϕ. This is directly related to the simultaneous decrease in η_m. Finally, for $\phi = 0.57$, not all of the injected fuel is consumed. There is hence a limit $\phi_c^{\max}$ on the amount of fuel that can be combusted without fuel waste, and we find $\phi_c^{\max} \approx 0.40$.

E. Influence of Boundary Conditions

Some data that cannot be directly measured need to be prescribed in the simulation: e.g., M_{H_2} and the wall temperatures. We discussed our choices for these variables in Sec. III and now evaluate this choice. Figure 6a shows $\tilde{p}$ for $M_{H_2} = 0.7, 1.0, 1.5, 2.6$. The curves for $M_{H_2} \leq 1.5$ are almost identical. Only the data for $M_{H_2} = 2.6$ show increased pressure levels, but the differences to the other curves are small. Figure 6b shows η_c for the M_{H_2} from Fig. 6a. For $M_{H_2} > 1$, the combustion process is faster. However, for $M_{H_2} \leq 1$, the curves are almost identical. Hence, $M_{H_2} = 1$ is a conservative estimate with regard to η_c. This is also true for η_m. Figures 6a and 6b also contain the results for the case of adiabatic walls. Here, peak wall temperatures reach values larger than 2700 K. Wall pressures are little higher in the injector wake than for the reference case and there is some influence on the flow conditions upstream of the injector leading edges. However, the peak pressure levels and the pressure

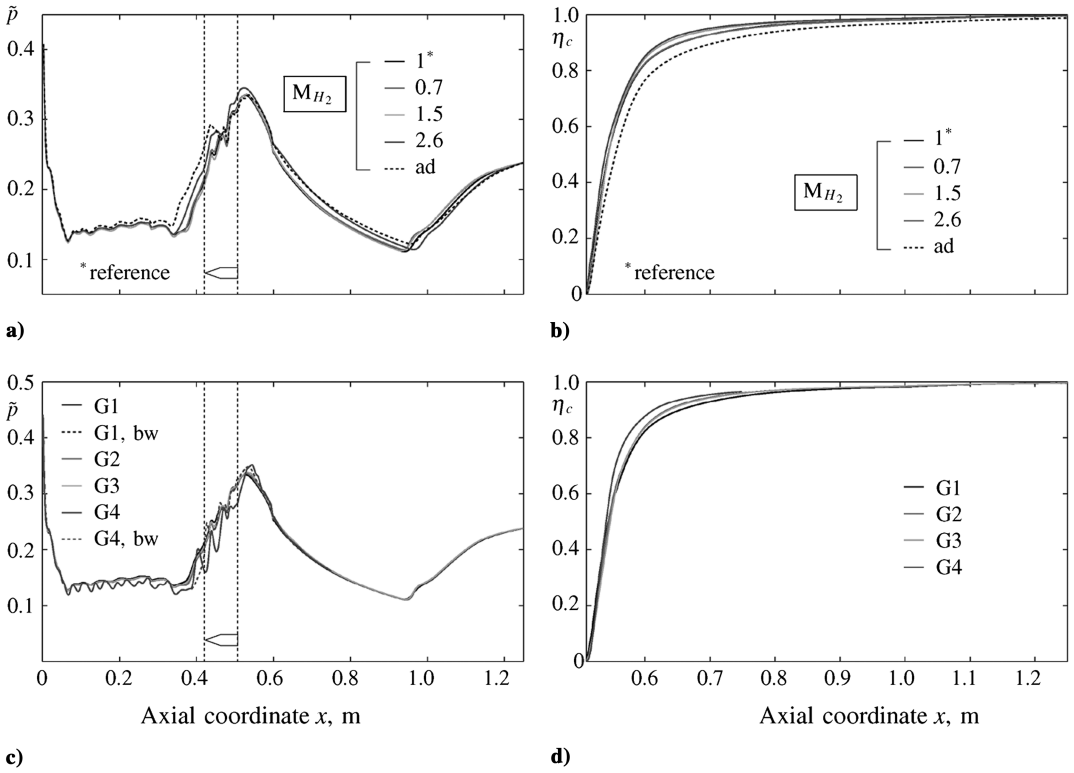

Fig. 6 Plots of a) $\tilde{p}$ and b) η_c for different M_{H_2} and the case of adiabatic walls (ad is adiabatic walls), c) $\tilde{p}$ and d) η_c for the various grids (bw is bottom wall); also see Table 2.

levels in the isolator remain virtually unchanged. Based on this, it is difficult to make any prediction with regard to actual wall temperatures. The differences in η_c are not significant when compared with the reference case, but we do observe a small decrease for adiabatic walls. Cooled walls should hence positively affect η_c.

F. Grid Sensitivity

Figure 6c shows $\tilde{p}$ for G1, G2, G3, and G4. For G1 and G4, $\tilde{p}$ is also given on the bottom wall. The distributions on G1, G2, and G3 are very similar and the curves on the top and bottom walls are essentially identical on G1. However, G4 shows some differences. On the upper wall, we find significant variations in $\tilde{p}$, which are due to the shock systems in the isolator and around the injector. The curve for the bottom wall here is more similar to the data for G1, G2, and G3 than the curve for the upper wall. In the isolator, $\tilde{p}$ is lower than for the other grids, because the boundary layers are thinner. Therefore, loss estimates are conservative on the coarser grids. The regular variations in the isolator indicate that the shock system is better resolved on G4. Figure 6d shows the results for η_c. For G1, it is smaller than for the other grids, while the curves for G2 and G3 are similar. As before, this suggests that predictions for η_c are conservative on G1. This is, in fact, also true for η_m.

VI. Conclusions

A model scramjet combustor was studied numerically. The results showed reasonable agreement with experimental data. However, some local deviations are observed, which is probably due to incorrect predictions of boundary layers, deficiencies in shock capturing, insufficient resolution of expansion waves, and shortcomings in turbulence modeling. In summary, the results suggest that design studies for model supersonic combustion chambers can be carried out with simplified approaches using state-of-the art commercial software packages, but some local flow features will be missed.

Acknowledgment

This study was carried out under a research grant from the German Research Foundation (DFG) within the framework of the research training group GRK1095/1. This support is gratefully acknowledged.

References

[1] Chun, J., Scheuermann, T., von Wolfersdorf, J., and Weigand, B., "Experimental Study on Combustion Mode Transition in a Scramjet with Parallel Injection," 14th AIAA/AHI Space Planes and Hypersonic Systems and Technologies Conference, AIAA Paper 2006-8063, Canberra, Australia, Nov. 2006.

[2] Gerlinger, P., Kasal, P., Schneider, F., von Wolfersdorf, J., Weigand, B., and Aigner, B., *Basic Research and Technologies for Two-Stage-to-Orbit Vehicles*, Wiley-VCH Verlag, Berlin, 2005, pp. 365–382.

[3] Gerlinger, P., Stoll, P., Kindler, M., Schneider, S., and Aigner, M., "Numerical Investigation of Mixing and Combustion Enhancement in Supersonic Combustors by Strut Induced Streamwise Vorticity," *Aerospace Science and Technology*, Vol. 12, No. 2, March 2008, pp. 159–168. doi:10.1016/j.ast.2007.04.003

[4] Scheuermann, T., Chun, J., and von Wolfersdorf, J., "Experimental Investigations of Scramjet Combustor Characteristics," 15th AIAA International Space Planes and Hypersonic Systems and Technologies Conference, AIAA Paper 2008-2552, Dayton, OH, April 2008.

[5] CFD++, Software Package, Ver. 6.1.1, Metacomp Technologies Inc., Agoura Hills, CA, 2007.

[6] Goldberg, U., Peroomian, O., and Chakravarthy, S., "Validation of CFD ++ Code Capability For Supersonic Combustor Flowfields," 33rd AIAA/ASME/SAE/ASEE Joint Propulsion Conference and Exhibit, AIAA Paper 1997-3271, Seattle, WA, July 1997.

[7] Goldberg, U., Batten, P., Palaniswamy, S., Chakravarthy, S., and Peroomian, O., "Hypersonic Flow Predictions Using Linear and Nonlinear Turbulence Closures," *Journal of Aircraft*, Vol. 37, No. 4, July–Aug. 2000, pp. 671–675. doi:10.2514/2.2650

[8] Goldberg, U., "Hypersonic Flow Heat Transfer Prediction Using Single Equation Turbulence Models," *Journal of Heat Transfer*, Vol. 123, No. 1, Feb. 2001, pp. 65–69. doi:10.1115/1.1337653

[9] Goldberg, U., Batten, P., and Palaniswamy, S., "The *q-l* Turbulence Closure for Wall-Bounded and Free Shear Flows," 42nd AIAA Aerospace Sciences Meeting and Exhibit, AIAA Paper 2004-269, Reno, NV, Jan. 2004.

[10] Palaniswamy, S., Goldberg, U., Peroomian, O., and Chakravarthy, S., "Predictions of Axial and Transverse Injection into Supersonic Flow," *Flow, Turbulence and Combustion*, Vol. 66, No. 1, January 2001, pp. 37–55. doi:10.1023/A:1011479002452

[11] Gerlinger, P., Möbus, H., and Brüggemann, D., "An Implicit Multigrid Method for Turbulent Combustion," *Journal of Computational Physics*, Vol. 167, 2001, pp. 247–276. doi:10.1006/jcph.2000.6671

C. Segal
Associate Editor